inorganics

MDPI

Article

Single-Atom Cobalt-Doped 2D Graphene: Electronic Design for Multifunctional Applications in Environmental Remediation and Energy Storage

Zhongkai Huang [1,*], Yue Zhang [1], Chunjiang Li [1], Liang Deng [1], Bo Song [1], Maolin Bo [1], Chuang Yao [1], Haolin Lu [2] and Guankui Long [2,*]

[1] Key Laboratory of Extraordinary Bond Engineering and Advanced Materials Technology of Chongqing, Yangtze Normal University, Chongqing 408100, China; yuezhang0922@163.com (Y.Z.); lichunjiang2004@163.com (C.L.); dengliangacademic@163.com (L.D.); songboacademic@163.com (B.S.); bmlwd@yznu.edu.cn (M.B.); yaochuang@yznu.cn (C.Y.)

[2] Renewable Energy Conversion and Storage Center (RECAST), National Institute for Advanced Materials, School of Materials Science and Engineering, Nankai University, Tianjin 300350, China; 1713638@mail.nankai.edu.cn

* Correspondence: zhongkaihuang@yznu.edu.cn (Z.H.); longgk09@nankai.edu.cn (G.L.)

Abstract

Through atomic-scale characterization of a single cobalt atom anchored in a pyridinic N_3 vacancy of graphene (Co-N_3-gra), this study computationally explores three interconnected functionalities mediated by cobalt's electronic configuration. Quantum-confined molecular prototypes extend prior bulk models, achieving a competitive catalytic activity for CO oxidation via Langmuir–Hinshelwood pathways with a 0.85 eV barrier. These molecular prototypes' discrete energy states facilitate single-electron transistor operation, enabling sensitive detection of NO, NO_2, SO_2, and CO_2 through adsorption-induced conductance modulation. When applied to lithium–sulfur batteries using periodic Co-N_3-gra, cobalt sites enhance polysulfide conversion kinetics and suppress the shuttle effect, with the $Li_2S_2 \rightarrow Li_2S$ step identified as the rate-limiting process. Density functional simulations provide atomic-scale physicochemical characterization of Co-N_3-gra, revealing how defect engineering in 2D materials modulates electronic structures for multifunctional applications.

Keywords: 2D material defects; electronic structure engineering; environmental gas sensors; lithium–sulfur batteries; structure–property relationships

check for updates

Academic Editors: Martina Vrankić and Melita Menelaou

Received: 12 August 2025
Revised: 9 September 2025
Accepted: 22 September 2025
Published: 24 September 2025

Citation: Huang, Z.; Zhang, Y.; Li, C.; Deng, L.; Song, B.; Bo, M.; Yao, C.; Lu, H.; Long, G. Single-Atom Cobalt-Doped 2D Graphene: Electronic Design for Multifunctional Applications in Environmental Remediation and Energy Storage. *Inorganics* **2025**, *13*, 312. https://doi.org/10.3390/inorganics13100312

Copyright: © 2025 by the authors. Licensee MDPI, Basel, Switzerland. This article is an open access article distributed under the terms and conditions of the Creative Commons Attribution (CC BY) license (https://creativecommons.org/licenses/by/4.0/).

1. Introduction

The concept of single-atom catalysis has emerged as a powerful strategy for achieving high activity and selectivity [1]. Leveraging its unique electronic configuration and tunable coordination chemistry, single-atom cobalt (Co) [2] emerges as a versatile platform spanning heterogeneous catalysis to quantum electronics. Beyond catalytic carbon oxide (CO) oxidation [3], Co sites exhibit non-sequential electron transport in single-electron transistors (SETs) [4], while analogous charge modulation enables molecular sensing [5,6] and energy storage catalysis [7]. This multifunctionality positions cobalt as a key building block for integrated environmental and energy technologies.

The exceptional activity of atomic Co catalysts originates from tunable coordination environments that optimize adsorption/desorption kinetics—critical for applications like pollutant degradation [8,9]. While Co-based systems show broad catalytic versatility (e.g., hydroformylation [10–14], and C-H activation [15–18]), their efficacy in gaseous pollutant

elimination remains underexplored. In 2016, Zhang et al. pioneered single Co atoms in pyridinic N_3 graphene (Co-N_3-gra), demonstrating efficient CO oxidation via Langmuir–Hinshelwood pathways with a 0.86 eV barrier [19].

However, two fundamental questions arise from this work [19]: How do quantum confinement effects in nanoscale Co-N_3-gra flakes modify electronic structures and catalytic behavior? Can the charge transfer mechanisms governing catalysis enable other functionalities like sensing and energy storage? Addressing these gaps requires multiscale computational probes bridging discrete and periodic systems.

The discrete energy states of quantum-confined flakes provide an ideal platform for SETs. When configured with Co-based islands [20,21], SETs resolve single-electron charging effects through Coulomb blockade phenomena—including quantized charge states and stability diamonds—that fingerprint molecular energy landscapes [22,23]. This approach offers direct electrical readouts of electronic states complementary to spectroscopic methods.

Molecular adsorption at Co sites enables environmental monitoring, particularly for bioactive gases (NO/NO_2) [24,25] and pollutants (CO_2/SO_2) [26]. Crucially, adsorption-induced conductance shifts in SETs directly correlate with charge redistribution during catalytic activation. For instance, NO_2 adsorption triggers electron transfer analogous to O_2 activation in CO oxidation, establishing SETs as in situ probes of catalytic behavior.

In energy storage, lithium–sulfur(Li-S) batteries face challenges from polysulfide shuttling [27,28]. Recent advances highlight the promise of two-dimensional (2D) layered nitrogenous carbon-based material for suppressing the polysulfide shuttle effect in Li-S batteries [29]. Unlike prior nanoparticle approaches [7,30,31], we pioneer periodic Co-N_3-gra for Li-S systems—retaining identical coordination while enabling electrode-scale simulations. Co-based catalysts enhance polysulfide conversion [32–34] and improve conductivity [7,32,35,36], directly translating electronic insights from flakes to practical interfaces.

Through density functional theory (DFT), this work implements a three-tier strategy: revisiting CO oxidation on a quantum-confined Co-N_3-gra molecular prototype to probe size effects, employing SETs to quantify charge states and adsorption behavior, and applying these insights to Li-S catalysis via periodic Co-N_3-gra models. Rather than treating these applications in isolation, this work seeks to demonstrate a unified design principle: the electronic structure of the atomically dispersed cobalt site serves as a universal 'control knob' for diverse functionalities. Section 3 details computational methods, with results progressing systematically from catalysis (Section 2.1) to SET characterization (Section 2.2), molecular sensing (Section 2.3), and Li-S battery applications (Section 2.4). Section 4 summarizes how charge redistribution unifies functionality across systems.

2. Results and Discussion

2.1. Catalytic Design for Environmental Remediation

In this section, the catalytic effect of the single Co atom embedded in pyridinic nitrogen vacancy sites in graphene molecular prototype (Co-N_3-gra molecular prototype) on CO is investigated for the first time, as far as we know. As shown in Equations (1) and (2), CO can be oxidized in two reactions:

$$CO + O_2 \xrightarrow{Co} CO_2 + O, \quad (1)$$

$$CO + O \xrightarrow{Co} CO_2. \quad (2)$$

The catalytic oxidation of CO (Equation (1)) was investigated through two well-established pathways: the Eley–Rideal (ER) and LH mechanisms [37]. In the ER pathway, CO molecules from the gas phase react directly with pre-adsorbed oxygen molecules on the

cobalt site, forming a carbonate-like intermediate that undergoes subsequent dissociation. By contrast, the LH mechanism initiates with co-adsorbed CO and O_2 species that undergo intramolecular rearrangement before decomposing through a peroxide-like intermediate. Following CO_2 desorption, the residual atomic oxygen on the cobalt center retains catalytic activity, enabling continuous oxidation cycles through Equation (2) with minimal energy penalty.

The reaction adsorption energy is calculated using the following formula:

$$E_{ads} = E_{total} - E_{adsorbate} - E_{cluster} \quad (3)$$

where E_{ads}, E_{total}, $E_{adsorbate}$, $E_{cluster}$ denote the energies adsorbed on the Co atoms, total energy of combined cluster-and-adsorbate complex, the energy of the isolated adsorbate, and the energy of the isolated cluster model itself (e.g., the $CoC_9N_3H_9$ molecular prototype), respectively. Note that $E_{cluster}$ represents the entire supported active site, not just the single metal atom.

The energy barriers mentioned above were evaluated at zero Kelvin (0 K). However, to account for the effects of temperature, the free-energy changes (ΔG) of the processes need to be corrected, resulting in the adjusted energy barriers E'_{bar}. The adjusted energy barriers can be calculated using the equation $\Delta G = \Delta H - T\Delta S$, where ΔH the change in enthalpy, T is the room temperature (298.15 K), and ΔS is the change in entropy. Given that $\Delta H = \Delta U - P\Delta V$, $\Delta U = \Delta E_{tot} + \Delta E_{vib} + \Delta E_{trans} + \Delta E_{rot}$ and $\Delta S = \Delta S_{vib} + \Delta S_{trans} + \Delta S_{rot}$, where ΔU is the change in internal energy, ΔE_{tot} is the change in total electronic energy obtained from DFT calculations, and the subscripts vib, trans, and rot represent the vibrational, translational, and rotational components, respectively.

In the CO oxidation process, the ER mechanism is followed. As described in previous studies [19,38], this process consists of multiple steps and involves various intermediate products. Every reaction step is characterized by a different transition state, such as the transition state in step 1 of Equation (1) labeled as TS1 in Figure 1a, and that in step 2 of Equation (1) noted by TS2 in Figure 1b. In the initial step (Figure 1a), the reaction begins with physically adsorbed CO molecules, which gradually approach the O_2 molecules on the Co surface. During the transition from the initial state (IS) to the TS, the O-O bond elongates from 1.39 Å to 2.67 Å , requiring an energy barrier of 0.91 eV to be overcome. Subsequently, the system enters an intermediate state (MS), forming a carbonate-like structure, which is accompanied by the cleavage of one O-O bond and the formation of two C-O bonds.

As shown in Figure 1b, the reaction proceeds further. From the MS to the TS2, an energy barrier of 1.48 eV needs to be overcome, ultimately leading to the formation of a CO_2 molecule. Adsorption energy of -0.269 eV is consistent with typical van der Waals interactions, confirming the physical nature of the binding in the final state (FS). It is worth noting that the energy of the MS is 0.96 eV lower than that of the FS, making MS more stable. From a thermodynamic perspective, this stability hinders the spontaneous desorption of the generated CO_2 molecule, which is consistent with the results of other related studies [19]. Thus, the quite big barriers of CO_3 formation and dissociation indicate that the CO oxidation on Co-N3-gra molecular prototype via the ER mechanism is difficult.

In the LH mechanism, when transitioning from IS to MS, an energy barrier of 1.21 eV needs to be overcome. When FS is formed, the O-O bond is stretched from 1.521 Å to 1.968 Å. Subsequently, CO_2 begins to dissociate. After overcoming an energy barrier of 0.28 eV, the O-O bond is broken, forming TS2 where the distance between C and Co is 2.408 Å, as shown in Figure 2. After that, the C-Co bond breaks, and CO_2 is successfully dissociated, generating FS where the distance between C and Co is 4.258 Å. The energy released in the entire process is 0.21 eV. Comparative analysis between ER and LH mechanisms reveals distinct energetic landscapes for these routes; the LH pathway demonstrates superior

kinetics due to its lower activation barrier of 0.85eV after temperature corrections and energy-favorable dissociation between formed CO_2 and the Co-N_3-gra molecular prototype. This calculated barrier is competitive with experimental values reported for noble metal catalysts, such as Pt-based systems (1.0 eV) [39].

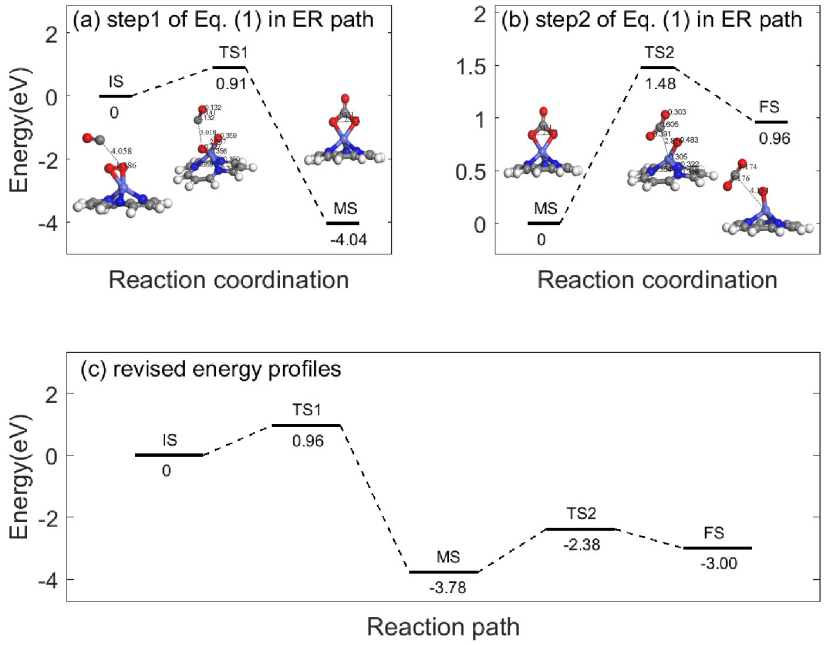


Figure 1. Catalytic reaction's energy profiles for CO oxidation over Co-$_3$-gra molecular prototype with the ER mechanism. (**a**) Initial step of Equation (1) transitions from IS to MS via TS1. (**b**) Second step of Equation (1) moves from MS to FS via TS2. (**c**) Revised energy profile including temperature corrections. Red, gray, deep blue, light blue, and white color balls in the figures represent oxygen, carbon, nitrogen, cobalt, and hydrogen atoms, respectively.

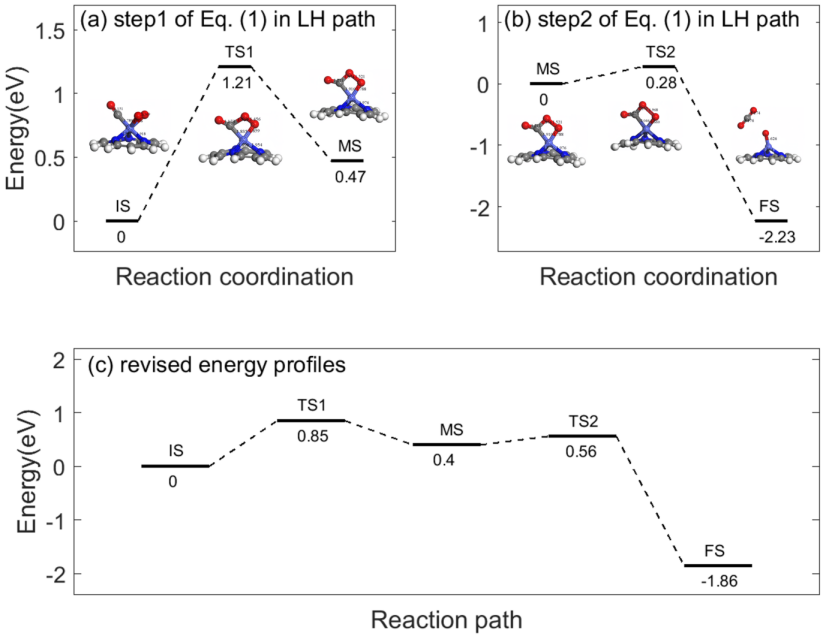


Figure 2. Catalytic reaction's energy profiles for catalytic CO oxidation over Co-$_3$-gra molecular prototype with the LH mechanism. (**a**) Initial step of Equation (1) transitions from IS to MS via TS1. (**b**) Second step of Equation (1) moves from MS to FS via TS2. (**c**) Revised energy profile including temperature corrections.

Following Equation (1) discussed above, there is an oxygen ion remaining on the Co atom. In the reaction described by Equation (2), an oxygen ion on the Co surface reacts with another CO molecule to form CO_2, with an energy barrier of 0.50 eV to be overcome (Figure 3a). The transition state in step 1 of Equation (2) is given by TS in Figure 3. This step releases an energy of 1.65 eV, which is significantly higher than the physisorption energy of CO_2 in the final state (FS) at 0.006 eV, indicating that the desorption of CO_2 is feasible [19]. Additionally, the validity of Equation (2) is supported by the reaction pathway in Equation (2) that starts with oxygen atoms [40].

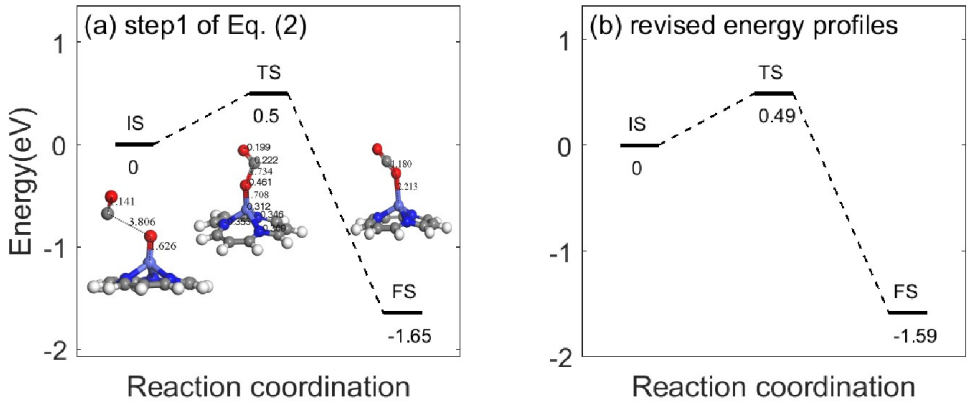


Figure 3. (**a**) Catalytic reaction's energy profiles for Equation (2) advances from IS to FS through TS. (**b**) Revised energy profile including temperature corrections.

The reaction paths following Equation (1) with LH mechanism and Equation (2) are thermally favorable, compared with those with ER mechanism. Partial density of states (PDOS) analysis for the LH mechanism and Equation (2) is given in Appendix A.1. It is also shown that inclusion of van der Waals interactions via DFT-D method does not alter the overall trends or conclusions of the active reaction pathways (LH and Equation (2)), as given in Appendix A.2. Reaction time for Figures 2a,b and 3a at room temperature is estimated by the following equation:

$$\tau = \nu^{-1} \exp\left(\frac{E_{bar}}{k_B T}\right) \quad (4)$$

where ν is in order of 10^{12} Hz, and k_B is the Boltzmann constant. For Figures 2a,b and 3a, we can obtain $\tau_1 = 2.33 \times 10^{-2}$ s, $\tau_2 = 2.9 \times 10^{-3}$ s, and $\tau_3 = 1.92 \times 10^{-4}$ s, respectively. Therefore, the adsorption of oxygen ions by Co exhibits fast reaction kinetics for CO oxidation, indicating rapid kinetics for oxygen–ion-mediated oxidation.

2.2. Single-Electron Phenomena in Defective 2D Graphene

In this study, the potential applications of Co atom-doped graphene in SETs were explored through theoretical simulations and calculations. Figure 4a depicts a schematic diagram of the SET device. A single Co atom-embedded pyridinic nitrogen-doped graphene molecular prototype is placed between two electrodes and serves as the central island for controlling the horizontal electron transport. The gate electrode is located below the central island, and the electron-transport characteristics are controlled by adjusting the gate voltage to achieve precise regulation of the electrical properties of the device [41,42].

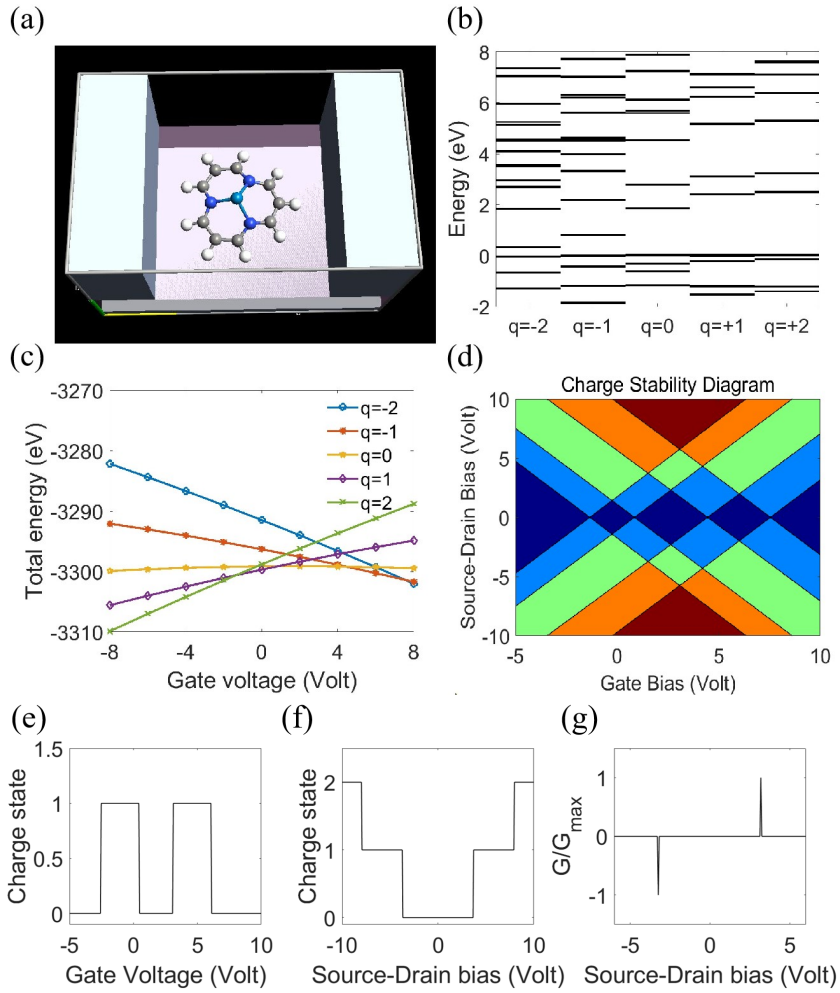


Figure 4. (**a**) The scheme of SET configuration with an island of a Co-N_3-gra molecular prototype, (**b**) the energy distribution across different charge states, (**c**) the influence of gate voltage on energy, and (**d**) voltage-dependent charge stability diagram for the Co-N_3-gra molecular prototype; the color scheme of dark blue, blue, green, orange, and red indicates the number of charge states of 0, 1, 2, 3, and 4, respectively. (**e**,**f**) Responses of charge states to gate voltage at fixed source-drain bias of 2.5 V, and its counterpart with fixed gate bias of −3.8 V, respectively, and (**g**) conductance under varying source-drain biases with fixed gate voltage of 0 V.

Figure 4b shows the energy distribution of Co atoms in different charge states. PDOS analysis for the neutral charge state is given in Appendix A.1. It can be seen that as the charge state changes from $q = -2$ to $q = +2$, the energy levels exhibit obvious quantization characteristics. In particular, when the charge states are $q = +1$ and $q = +2$, the energy levels are densely distributed near zero energy, indicating that these states are the most stable and most likely to be occupied under normal conditions. However, the energy levels for $q = -2$, $q = -1$, $q = 0$, and $q = +1$ are relatively sparse and far from the zero-energy level, suggesting that these states have higher energies and are less likely to be occupied under normal conditions. This discrete energy-level distribution enables Co atoms to exhibit single-electron charging behavior during the charge transfer process.

Figure 4c further shows the relationship between the total energy of Co atoms in the SET and the gate voltage. The total energy is a large negative value due to the sum of the energies of all electrons and nuclei in the system. The physically relevant information is the relative change in energy with gate voltage. As the gate voltage changes, the total energy under different charge states exhibits non-linear changes, which are closely related to the capacitive characteristics of the system. To gain additional insights into how total

energy varies with gate voltage and to explore the electronic properties of various central island configurations, we performed DFT calculations and fitted the results to a quadratic function: $E(q, V_g) = E_0 + qW + \alpha q V_g + \beta (eV_g)^2$ [32,41,42]. Here, $E(q, V_g)$ is the total energy of the SET with charge state q and gate voltage V_g. E_0 is a constant energy term, qW represents stored energy (a value of 5.28 eV is used to simulate gold electrodes), and $\alpha q V_g$ describes the linear coupling between the island and gate electrode. For Co, the parameters are $\alpha = 0.6477$ and $\beta = -0.0054$.

Figure 4d illustrates the charge stability diagram of the Co-based SET. With the source-drain bias voltage fixed, as the gate voltage is scanned, a series of periodic peaks can be observed, indicating that electrons are either added to or removed from the central island. These peaks form characteristic diamond-shaped regions in the $V_g - V_{sd}$ plane, constituting the charge stability diagram. The existence of these regions demonstrates the stability of the Co-based SET in different charge states [5], providing visual evidence for the charge control of the SET.

To better observe the performance of the SET, Figure 4e shows the variation of the charge state of the Co-N_3-gra molecular prototype with the gate bias under a fixed source-drain voltage of 2.5 volts, indicating that within a specific range of gate voltages, the Co-N_3-gra molecular prototype can stably maintain a single-charge state. Figure 4f presents the changes in the charge states under different source-drain biases at a fixed gate bias of −3.8 V. Figure 4g shows the variation of the maximum conductance of the Co-N_3-gra molecular prototype under different source-drain biases, and the Co-N_3-gra molecular prototype exhibits two conductance changes in the range from −5 V to 5 V.

The quantized charge states and gate-tunable energy levels reveal the discrete electronic structure of Co sites. This enables precise probing of electron transfer processes—a capability we leverage to investigate catalytic interactions with bioactive gases.

2.3. Catalytic Design for Environmental Remediation

In this part, building on the electronic state mapping of Co sites (Section 2.2), we employ SETs to detect bioactive gases through adsorption-induced conductance changes. As a highly sensitive device, the SET can detect the charge of a single electron, giving it a unique advantage in molecular adsorption detection.

Figure 5a illustrates the binding models of NO, NO_2, SO_2, and CO_2 gas molecules with Co atoms. The adsorption structures formed between different gas molecules and Co atoms are distinct. The Co complexes can be regarded as islands within the SET configuration. PDOS analysis for the four Co complexes is given in Appendix A.1, reflecting the crucial role of Co-N_3 center in molecule absorption. The selectivity between gas molecules is quantified with adsorption energies and charge transfer values in Appendix B.1. Due to the different interactions between the molecules and the SET, it is possible to evaluate their sensitivity to the adsorption of gas molecules.

Figure 5b shows the relationship between the charge states of different gas molecules in the SET as a function of gate voltage. It can be observed that the charge states of NO_2 and CO_2 molecules undergo significant changes at lower voltages as the gate voltage increases, while NO and SO_2 molecules require higher voltages to cause changes in their charge states. This indicates that NO_2 and CO_2 molecules have stronger interactions with cobalt atoms, which can more easily lead to electron transfer within the SET.

Figure 5c further demonstrates the changes in charge states of various gas molecules under different source-drain biases. The results show that SO_2 can achieve charge state transitions at smaller source-drain biases, while NO, SO_2, and CO_2 molecules require larger biases, consequently. Figure 5d shows the variation of normalized conductance of different

gas molecules in a SET with the source-drain bias, featuring distinct conductance peaks corresponding to specific air pollutants.

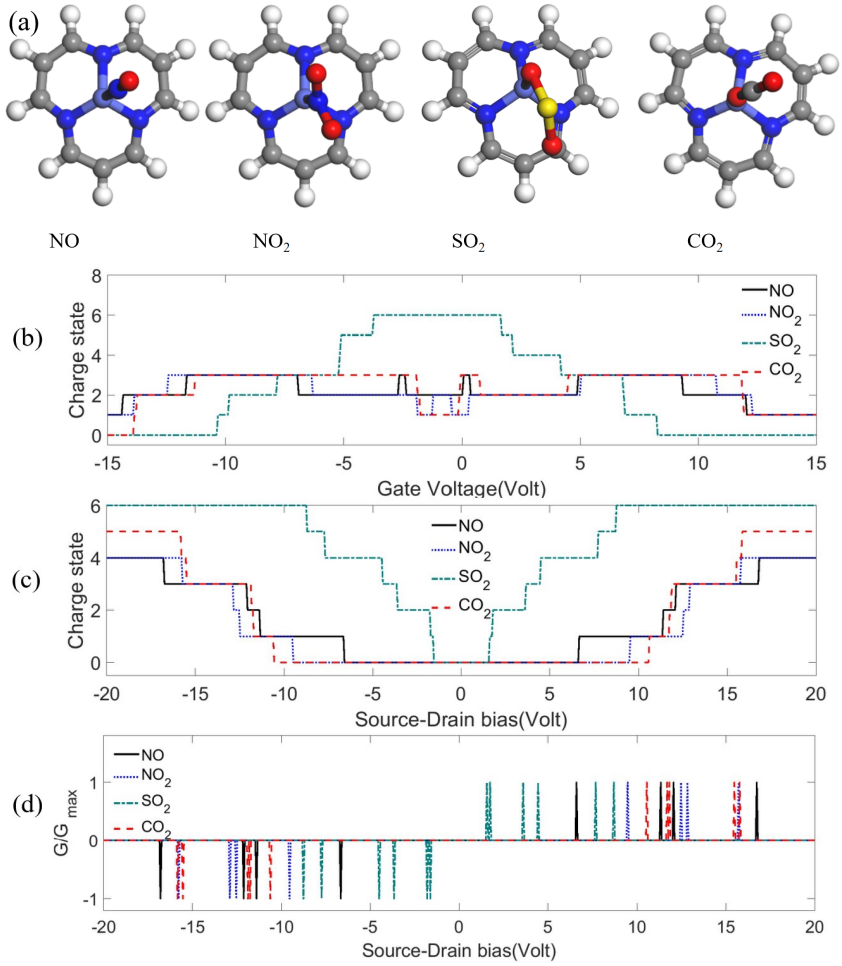


Figure 5. (**a**) Molecules of NO, NO_2, SO_2, and CO_2 adsorb onto the Co-N_3-gra molecular prototype. (**b**) Impact of gate voltage on charge state at fixed source-drain bias of −15 V. (**c**) Effect of source-drain voltage on charge state at fixed gate bias of 0 V. (**d**) Influence of source-drain voltage on conductivity at fixed gate bias of 0 V.

It is important to note that this study focuses on the fundamental charge transfer-based sensing mechanism. Translating this principle into a practical device would necessitate addressing several engineering challenges, including the fabrication of large-scale, uniform arrays of Co-N_3 sites, the minimization of $1/f$ noise and charge noise in graphene-based SETs at room temperature, and ensuring long-term stability against oxidation and poisoning. Nonetheless, quantifying the intrinsic electronic response, as done here, is a critical first step for identifying promising material candidates for next-generation sensors.

Co-N_3-gra can also be used to detect more complex molecules containing hydrocarbon radicals such as methanol, ethanol, butanol, etc., which are extremely important for many practical applications [43–45]. A detailed study can be found in Appendix B.2. The unique structural and electrical response characteristics of Co atoms' adsorption to different air pollutant molecules provide a theoretical basis for the development of highly sensitive air pollutant molecule detection devices based on Co atoms.

2.4. Stepwise Polysulfide Conversion Catalyzed by Atomic Cobalt Centers

Effective suppression of the polysulfide shuttle effect in Li-S batteries necessitates strong anchoring of lithium polysulfides (LiPSs). During discharge, sulfur undergoes stepwise re-

duction through adsorbed intermediates: S_8*→Li_2S_8*→Li_2S_6*→Li_2S_4*→Li_2S_2*→Li_2S* where asterisks denote binding at Co-N_3-gra catalytic sites (Figure 6). PDOS analysis for Li_2S* represents the key of Co-N_3 center in anchoring of the LiPs, as given in Appendix A.1. This cascade serves as an ideal model system for probing how atomically dispersed Co catalysts control reaction kinetics and thermodynamics in multielectron transfer processes.

The overall discharge process involves the reduction of adsorbed sulfur: S_8 + 16Li^+ + 16e^-→8Li_2S, which encompasses multiple elementary steps with associated intermediates [46]. To resolve the catalytic function of atomic Co sites, we decompose this process into five concerted reactions:

$$S_8 * + 2Li^+ + 2e^- \xrightarrow{Co} Li_2S_8 * \quad (5)$$

$$Li_2S_8 * + 4Li^+ + 4e^- \xrightarrow{Co} Li_2S_6 * + 2Li_2S, \quad (6)$$

$$Li_2S_6 * + 4Li^+ + 4e^- \xrightarrow{Co} Li_2S_4 * + 2Li_2S, \quad (7)$$

$$Li_2S_4 * + 4Li^+ + 4e^- \xrightarrow{Co} Li_2S_2 * + 2Li_2S, \quad (8)$$

$$Li_2S_2 * + 2Li^+ + 2e^- \xrightarrow{Co} Li_2S * + Li_2S, \quad (9)$$

where each step occurs at the Co-N_3 active sites.

To gain deeper mechanistic insights into polysulfide conversion catalyzed by Co-N_3-gra, we systematically evaluated the Gibbs free-energy landscape for the sulfur reduction pathway. The computational hydrogen electrode approach [47] was employed to determine the free-energy change (ΔG) for each elementary step according to

$$\Delta G = \Delta E + \Delta ZPE - T\Delta S. \quad (10)$$

In this expression, ΔE represents the reaction energy computed via DFT, ΔZPE accounts for zero-point energy (ZPE) variations, ΔS corresponds to entropy adjustments, and T denotes the absolute temperature. Thermodynamically favorable processes exhibit negative ΔG values (exergonic), whereas positive ΔG indicates endergonic reactions requiring energy input. As demonstrated in Figure 7, all five lithium polysulfide formation reactions maintain negative free-energy values throughout the 0–500 K temperature range, confirming their spontaneous character under battery operating conditions.

Under typical battery operating conditions (ambient temperature, 293 K), the free-energy profile for sulfur reduction on Co-N_3-gra reveals critical insights (Figure 8). The initial S_8*→Li_2S_8* conversion exhibits the most negative ΔG (−1.82 eV), confirming its exothermic and spontaneous nature. Analysis of the complete reaction pathway identifies the Li_2S_2*→$Li_2$2S* transition as kinetically limiting, with a substantial positive barrier of 3.52 eV— significantly higher than other elementary steps. This kinetic bottleneck originates from the solid–solid restructuring required for Li_2S_2 to Li_2S conversion, whereas preceding transitions involve more facile phase changes, including S_8*→ Li_2S_4* as a dissolution-mediated solid-to-liquid transition, Li_2S_4*→Li_2S_2* as a liquid-to-solid precipitation, and Li_2S_2 to Li_2S as a solid–solid crystal transformation. Such phase-dependent barriers align with experimental reports of nucleation-limited kinetics in sulfur cathodes [48]. This barrier value is higher than barriers reported for other cobalt-based catalysts (e.g., 1.38 eV on Co(111) [49]), suggesting our Co-N_3 site needs further optimization. Future catalyst design should therefore focus on optimizing Co-S bonding interactions through coordination engineering to facilitate this critical solid-state conversion.

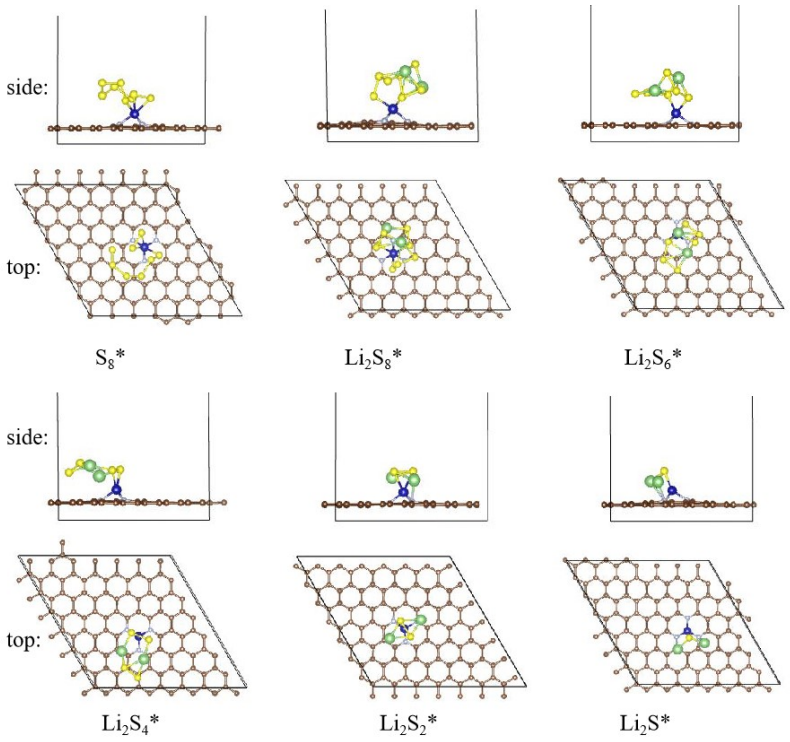


Figure 6. Side and top views of optimized geometrical configurations of sulfur species on Co-N_3-gra surfaces. Brown, blue, green, and yellow color balls represent carbon, cobalt, lithium, and sulfur atoms, respectively.

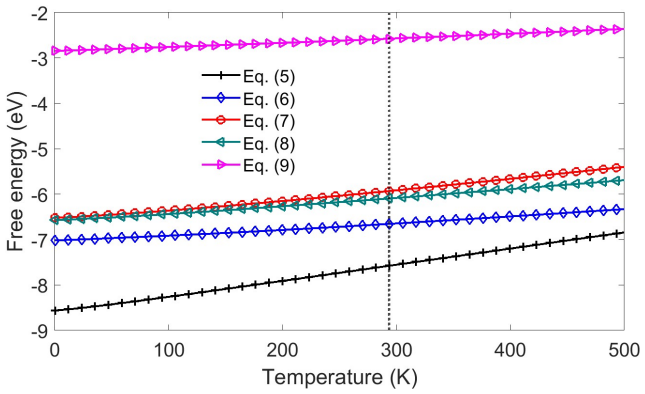


Figure 7. The Gibbs free-energy profile for Equations (5)–(9) from 0 to 500 K. The dotted vertical line marks the temperature of 293 K.

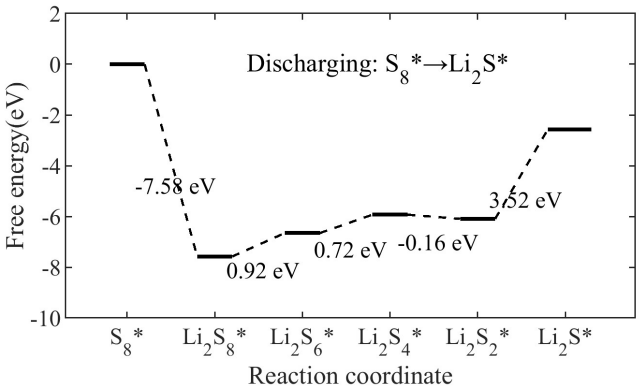


Figure 8. The Gibbs free-energy profile of LiPS species on the surface of Co-CN_3-gra in the LiPS reduction process at the temperature of 293K.

3. Materials and Methods

In the study of properties and catalytic applications of Co atom-doped graphene, spin-unrestricted DFT is employed. The computational setup was designed to ensure both accuracy and efficiency for the diverse systems studied, ranging from molecular clusters to periodic surfaces and transport devices.

3.1. Model Systems and Computation Details

In the work, two distinct types of models were utilized, depending on the application.

3.1.1. Molecular Cluster Models (for CO Oxidation, SET, and Molecular Sensing)

The active site was modeled using a $CoC_9N_3H_9$ molecular cluster (as shown in Figures 1–5), representing a single cobalt atom anchored in a pyridinic N_3 vacancy within a finite graphene molecular prototype. This cluster size was carefully chosen to balance computational efficiency with the accurate representation of the electronic structure of the Co-N_3 center. For CO oxidation and gas adsorption energy calculations, computations were performed in the DMol3 module without periodic boundary conditions. This approach is standard for modeling isolated molecular reactions and is in agreement with conventional first-principles studies of Co-based absorption and catalysis [50,51]. For SET simulations, the $CoC_9N_3H_9$ molecule served as the central island. Neumann boundary conditions were adopted, following established first-principles modeling practices for molecular-scale electronic devices [41]. Simulations were conducted using QuantumATK software 2019, combining DFT with the non-equilibrium Green's function (NEGF) formalism. The DFT-NEGF method was used to investigate the charging energies in SETs, while self-consistent-charge DFT was employed to study the electronic properties of the Co atoms' structures [32,52], ensuring model stability and the accurate capture of discrete energy levels and Coulomb blockade effects.

3.1.2. Periodic Model (for Li-S Battery Applications)

A periodic model was constructed using a 7×7 graphene supercell (in-plane lattice parameter of 2.46 Å) with a single Co-N_3 center. A vacuum layer of 15 Åwas added along the z-direction to decouple the periodic slabs and prevent any spurious interactions between them, which is sufficient for convergence of the electronic structure.

3.2. Exchange-Correlation Functional and Basis Set

The Perdew–Burke–Ernzerhof (PBE) functional within the generalized gradient approximation (GGA) was employed for all calculations. While this functional possibly underestimates absolute reaction barriers, it provides a well-established and computationally efficient framework for describing catalytic reaction mechanisms [19], adsorption energetics, and electronic structures in carbon-based materials and transition-metal complexes, and its use is consistent with previous computational studies of cobalt-based catalysts [50,51]. The double numerical plus polarization (DNP) basis set was used throughout this work. The DNP basis set is the default in the DMol3 module, offering good accuracy in describing both the localized d-orbitals of the cobalt atom and the delocalized π-system of the graphene substrate. Grimme's DFT-D method was used to account for dispersion interactions. Core electrons were treated with DFT semi-core pseudopotentials (DSPPs) to account for relativistic effects [6,53–55].

3.3. Convergence Parameters and Transition State Search

During the calculations, the energy convergence tolerance was set to 5×10^{-7} Hartree, the maximum force to 0.005 Hartree/Å, and the displacement to 0.05 Å, to ensure the precision of the calculations. To determine the minimum energy path for the CO oxidation

reaction, the linear synchronous transit/quadratic synchronous transit (LST/QST) methods were utilized [56]. The vibrational frequencies were calculated to obtain the zero-point energy (ZPE) and thermal corrections to the Gibbs free energy.

4. Conclusions

This computational study demonstrates that the multifunctionality of single-atom cobalt-doped graphene stems from a common root: the tunable electronic structure of the Co-N_3 active site. The ability of this site to undergo charge redistribution enables it to facilitate catalytic cycles, alter conductance in SETs for sensing, and enhance reaction kinetics in batteries. Our key findings reveal that in catalytic applications, Co-N_3-gra molecular prototypes drive efficient CO oxidation via LH pathways, with the rate-limiting step exhibiting a 0.85 eV barrier. The coordination environment critically tunes reaction energetics, as shown in the contrasting mechanisms between ER and LH pathways. For electronic and sensing applications, quantum confinement in nanoscale molecular prototypes creates discrete energy states that enable precise SET operation. When configured as Coulomb islands, these systems detect adsorption events through characteristic conductance shifts—particularly for environmentally relevant gases like NO, NO_2, SO_2, and CO_2. In energy storage, periodic Co-N_3-gra models significantly mitigate the polysulfide shuttle effect in Li-S batteries. Our work identifies the $Li_2S_2 \rightarrow Li_2S$ conversion as the rate-limiting step and quantifies its challenging barrier, providing a key metric for future catalyst design. This work demonstrates that the electronic structure of a single Co-N_3 active site serves as a unified platform for multifunctional applications. We elucidate the mechanism by which charge redistribution at this specific site simultaneously governs its catalytic, sensing, and energy storage functionalities.

Author Contributions: Conceptualization, Z.H. and G.L.; methodology, Z.H. and L.D.; software, M.B. and C.Y.; validation, Y.Z., C.L. and L.D.; formal analysis, Z.H., L.D. and G.L.; investigation, Z.H., Y.Z., C.L., L.D., B.S. and H.L.; resources, G.L.; data curation, Y.Z., C.L., L.D. and B.S.; writing—original draft preparation, Y.Z.; writing—review and editing, Z.H.; visualization, Z.H., Y.Z. and C.L.; supervision, G.L.; project administration, Z.H. and G.L.; funding acquisition, Z.H. All authors have read and agreed to the published version of the manuscript.

Funding: This research was funded by the Science and Technology Research project of Chongqing Education Commission under No. KJQN202201421 and KJQN202401422, and the Fuling District guiding scientific research project under No. FLKJ.2024BAG5130.

Institutional Review Board Statement: Not applicable.

Informed Consent Statement: Not applicable.

Data Availability Statement: Data are contained within the article. Further inquiries can be directed to the corresponding author.

Acknowledgments: We would like to express our sincere gratitude to Yangtze Normal University and Nankai University for providing the equipment for this research.

Conflicts of Interest: The authors declare no conflicts of interest.

Appendix A. Electronic Structures Analysis

Appendix A.1. PDOS Analysis

Figure A1 clearly shows hybridization of d orbital of Co, CO, and O_2 during the LH catalytic circle. In the initial state, the O_2 molecule is significantly activated upon adsorption, as evidenced by the elongated O-O bond and the hybridization between Co-d orbitals and O_2 orbitals near the Fermi level. At the transition state, this hybridization intensifies, and a new emerging state indicates electron redistribution towards the formation of the peroxide-

like intermediate, concomitant with O-O bond weakening. Figure A2 displays the active charge redistribution for Co, CO, and O for the Equation (2) mechanism. The Co-adsorbed atomic oxygen site exhibits a highly reactive electronic state. This state readily interacts with the approaching CO molecule, leading to a low-barrier transition state characterized by Co-O-C hybridization. Comparing with Figure 2 and Figure 3 in the main context, the bond cleavage is accompanied by a significant charge redistribution, as revealed by our PDOS analysis above. The electronic structure evolution directly drives the catalytic cycle. Figures A3–A5 present the PDOS analysis for Co-N_3-gra molecular prototype as SET island, for NO, NO_2, SO_2, and CO_2 adsorbed onto the Co-N_3-gra molecular prototype, and for representative LiPs on Co-N_3 graphene, respectively. It can be found that Co serves as active sites due to clear hybridization between Co-d orbitals and neighboring states of atoms/molecules.

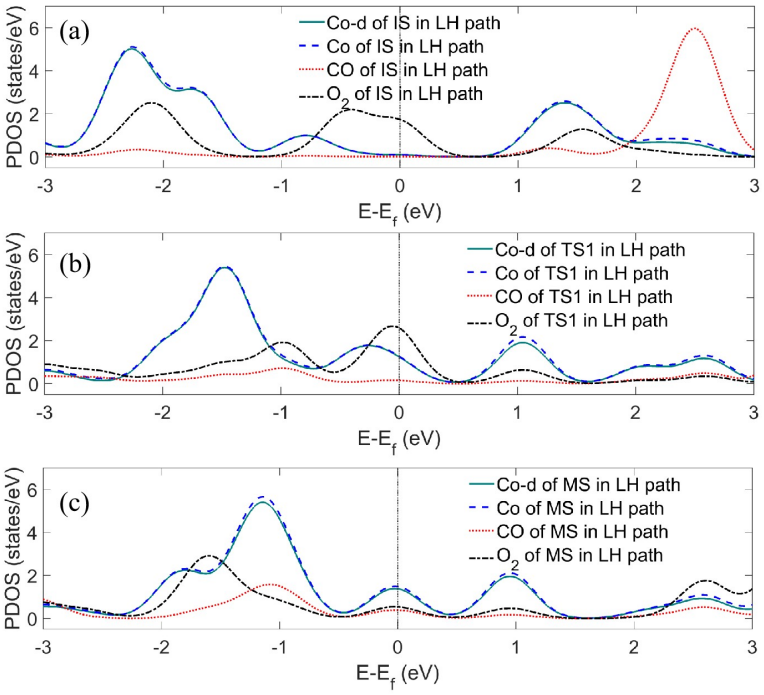


Figure A1. PDOS analysis for (**a**) IS, (**b**) TS1, and (**c**) MS in the LH path.

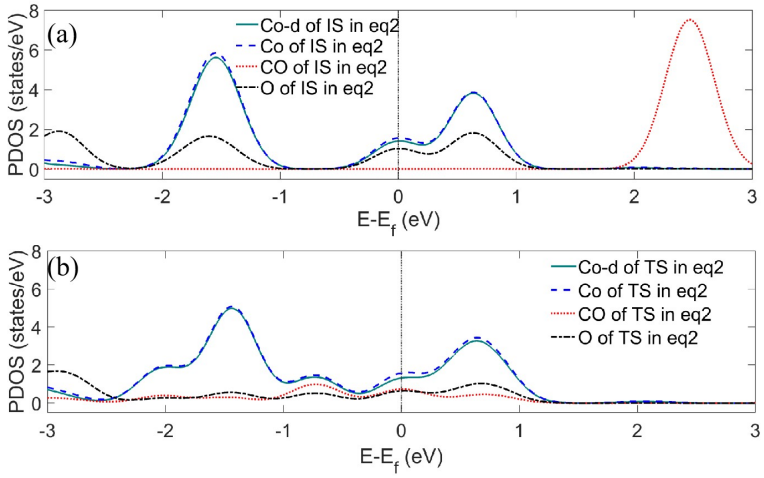


Figure A2. PDOS analysis for (**a**) IS and (**b**) TS in the path of Equation (2).

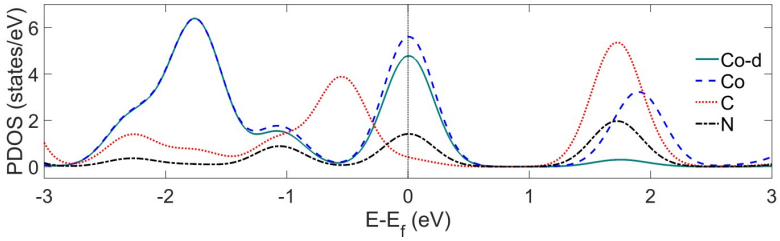


Figure A3. PDOS analysis for the Co-N_3-gra molecular prototype.

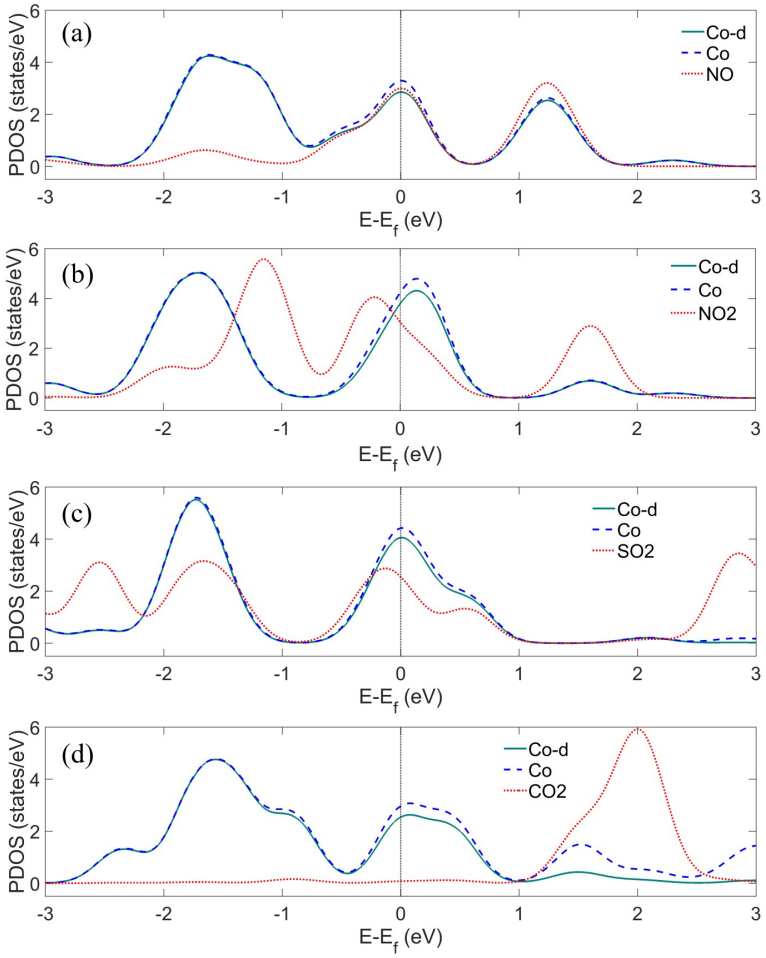


Figure A4. PDOS analysis for (**a**) NO, (**b**) NO_2, (**c**) SO_2, and (**d**) CO_2 adsorbed onto the Co-N_3-gra molecular prototype.

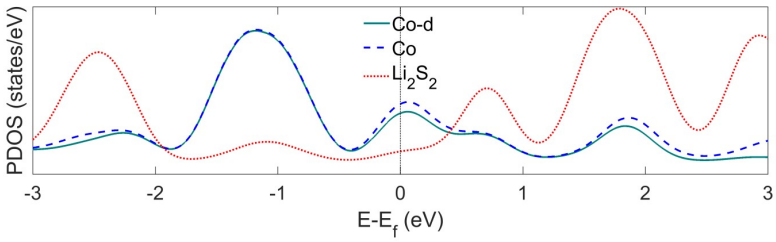


Figure A5. PDOS analysis for LiPs.

Appendix A.2. DFT-D Correction

Inclusion of vdW corrections does not alter the overall trends or conclusions of the active reaction pathways (LH and Equation (2)). The relative energy landscape and the identity of the rate-limiting step remain unchanged. The revised energy profiles (with vdW corrections) are now included in the Figures A6 and A7 for transparency.

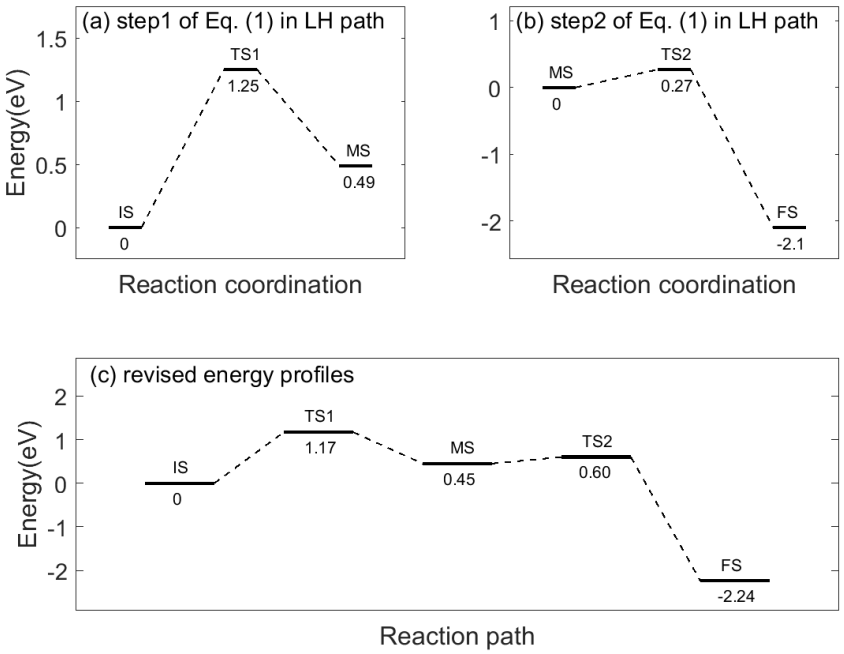


Figure A6. Catalytic reaction's energy profiles for catalytic CO oxidation over Co-$_3$-gra molecular prototype with the LH mechanism. (**a**) Initial step of Equation (1) transitions from IS to MS via TS1. (**b**) Second step of Equation (1) moves from MS to FS via TS2. (**c**) Revised energy profile including temperature corrections. Vdw correction is adopted for related calculations.

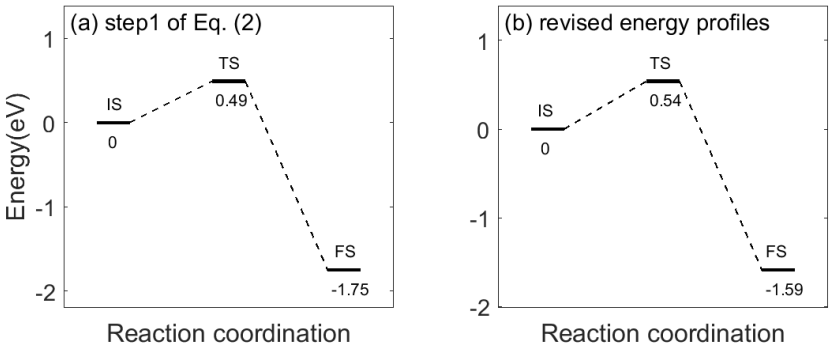


Figure A7. (**a**) Catalytic reaction's energy profiles for Equation (2) advance from IS to FS through TS. (**b**) Revised energy profile including temperature corrections. Vdw correction is adopted for related calculations.

Appendix B. Sensing

Appendix B.1. Charge Transfer Mechanism

The selectivity can be rigorously quantified by the adsorption strength and the amount of charge transfer, as summarized in the above figure. NO_2 exhibits the strongest adsorption (-0.128 eV), confirming it as the most sensitive analyte. This is followed by NO, SO_2, and CO_2, which correlates perfectly with the conductance shift trends in Figure 5. This quantitative analysis removes any ambiguity in the selectivity ordering. Furthermore, it directly links the sensing mechanism to the catalytic process: the strong charge transfer to NO_2 mirrors its role as an oxidant in catalytic cycles, unifying the functionality of the Co-N_3 site across different applications.

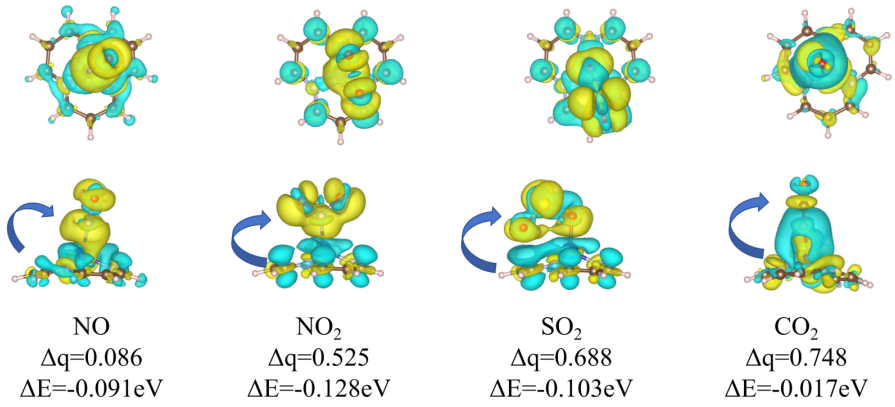


Figure A8. Charge density difference, absorption energy, and Bader charge for air pollutant sensing.

Appendix B.2. Detection of Hydrocarbon Radicals

This section illustrates the detection of more complex molecules containing hydrocarbon radicals such as methanol, ethanol, and butanol. Figure A9a illustrates the binding models of butanol, ethanol, and methanol molecules with the Co-N_3-gra molecular prototype. Figure A9b–d display the effect of gate voltage on charge state at fixed source-drain bias of −15 V, impact of source-drain voltage on charge state at fixed gate bias of 0 V, and influence of source-drain voltage on conductivity at fixed gate bias of 0 V, respectively. Due to the different interactions between the molecules and the SET, it is possible to evaluate their sensitivity to the adsorption of studied molecules.

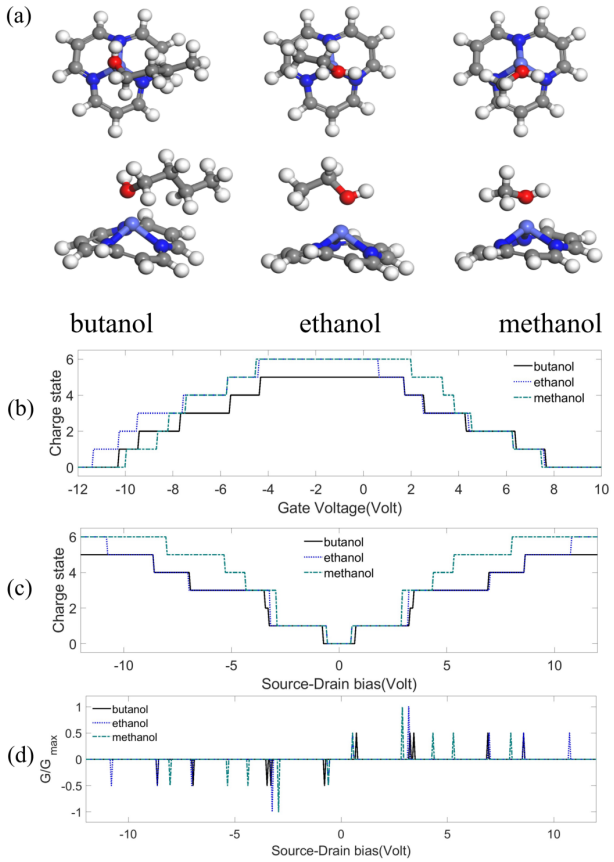


Figure A9. (**a**) Molecules of methanol, ethanol, and butanol adsorb onto the Co-N_3-gra molecular prototype. (**b**) Impact of gate voltage on charge state at fixed source-drain bias of −15 V. (**c**) Effect of source-drain voltage on charge state at fixed gate bias of 0 V. (**d**) Influence of source-drain voltage on conductivity at fixed gate bias of 0 V.

References

1. Yang, X.-F.; Wang, A.; Qiao, B.; Li, J.; Liu, J.; Zhang, T. Single-atom catalysts: A new frontier in heterogeneous catalysis. *Accounts Chem. Res.* **2013**, *46*, 1740–1748. [CrossRef] [PubMed]
2. Gambardella, P.; Rusponi, S.; Veronese, M.; Dhesi, S.S.; Grazioli, C.; Dallmeyer, A.; Cabria, I.; Zeller, R.; Dederichs, P.H.; Kern, K.; et al. Giant magnetic anisotropy of single cobalt atoms and nanoparticles. *Science* **2003**, *300*, 1130–1133. [CrossRef] [PubMed]
3. Ipadeola, A.K.; Chitt, M.; Abdelgawad, A.; Eid, K.; Abdullah, A.M. Graphene-based catalysts for carbon monoxide oxidation: Experimental and theoretical insights. *Int. J. Hydrogen Energy* **2023**, *48*, 17434–17467. [CrossRef]
4. Park, J.; Pasupathy, A.N.; Goldsmith, J.I. Coulomb blockade and the Kondo effect in single-atom transistors. *Nature* **2002**, *417*, 722–725. [CrossRef]
5. Rani, S.; Ray, S.J. Detection of gas molecule using C_3N island single electron transistor. *Carbon* **2019**, *144*, 235–240. [CrossRef]
6. Shabeeb, M.; Maity, S. Computational investigation on adsorption and activation of atmospheric pollutants co, no and so on small cobalt clusters. *Chem. Phys.* **2024**, *582*, 112291. [CrossRef]
7. Wang, F.; Li, J.; Zhao, J.; Yang, Y.; Su, C.; Zhong, Y.L.; Yang, Q.H.; Lu, J. Single-atom electrocatalysts for lithium sulfur batteries: Progress, opportunities, and challenges. *ACS Mater. Lett.* **2020**, *2*, 1450–1463. [CrossRef]
8. Ozols, K.; Jang, Y.S.; Cramer, N. Chiral cyclopentadienyl cobalt(iii) complexes enable highly enantioselective 3d-metal-catalyzed c-h functionalizations. *J. Am. Chem. Soc.* **2019**, *141*, 5675–5680. [CrossRef]
9. Cao, L.; Luo, Q.; Liu, W.; Lin, Y.; Liu, X.; Cao, Y.; Zhang, W.; Wu, Y.; Yang, J.; Yao, T.; et al. Identification of single-atom active sites in carbon-based cobalt catalysts during electrocatalytic hydrogen evolution. *Nat. Catal.* **2019**, *2*, 134–141. [CrossRef]
10. Hood, D.M.; Johnson, R.A.; Carpenter, A.E.; Younker, J.M.; Vinyard, D.J.; Stanley, G.G. Highly active cationic cobalt(ii) hydroformylation catalysts. *Science* **2020**, *367*, 542–548. [CrossRef]
11. MacNeil, C.S.; Mendelsohn, L.N.; Pabst, T.P.; Hierlmeier, G.; Chirik, P.J. Alcohol synthesis by cobalt-catalyzed visible-light-driven reductive hydroformylation. *J. Am. Chem. Soc.* **2022**, *144*, 19219–19224. [CrossRef]
12. Delolo, F.G.; Yang, J.; Neumann, H.; Dos Santos, E.N.; Gusevskaya, E.V.; Beller, M. Cobalt-catalyzed hydroformylation under mild conditions in the presence of phosphine oxides. *ACS Sustain. Chem. Eng.* **2021**, *9*, 5148–5154. [CrossRef]
13. Hebrard, F.; Kalck, P. Cobalt-catalyzed hydroformylation of alkenes: Generation and recycling of the carbonyl species, and catalytic cycle. *Chem. Rev.* **2009**, *109*, 4272–4282. [CrossRef] [PubMed]
14. Zhang, B.; Kubis, C.; Franke, R. Hydroformylation catalyzed by unmodified cobalt carbonyl under mild conditions. *Science* **2022**, *377*, 1223–1227. [CrossRef] [PubMed]
15. Gao, K.; Yoshikai, N. Low-valent cobalt catalysis: New opportunities for c-h functionalization. *Accounts Chem. Res.* **2014**, *47*, 1208–1219. [CrossRef]
16. Nakanowatari, S.; Mei, R.; Feldt, M.; Ackermann, L. Cobalt(iii)-catalyzed hydroarylation of allenes via c-h activation. *ACS Catal.* **2017**, *7*, 2511–2515. [CrossRef]
17. Oliveira, J.C.; Dhawa, U.; Ackermann, L. Insights into the mechanism of low-valent cobalt-catalyzed c-h activation. *ACS Catal.* **2021**, *11*, 1505–1515. [CrossRef]
18. Li, T.; Shen, C.; Sun, Y.; Zhang, J.; Xiang, P.; Lu, X.; Zhong, G. Cobalt-catalyzed olefinic c-h alkenylation/alkylation switched by carbonyl groups. *Org. Lett.* **2019**, *21*, 7772–7777. [CrossRef]
19. Zhang, X.; Lu, Z.; Yang, Z. Single non-noble-metal cobalt atom stabilized by pyridinic vacancy graphene: An efficient catalyst for co oxidation. *J. Mol. Catal. A Chem.* **2016**, *417*, 28–35. [CrossRef]
20. Hu, W.; Wang, C.; Tan, H.; Duan, H.; Li, G.; Li, N.; Ji, Q.; Lu, Y.; Wang, Y.; Sun, Z.; et al. Embedding atomic cobalt into graphene lattices to activate room-temperature ferromagnetism. *Nat. Commun.* **2021**, *12*, 1854. [CrossRef]
21. Gallagher, C.; Siddiqui, W.; Arnold, T.; Cheng, C.; Su, E.; Zhao, Q. Benchmarking a Molecular Flake Model on the Road to Programmable Graphene-Based Single-Atom Catalysts. *J. Phys. Chem. C* **2024**, *128*, 2876–2883. [CrossRef]
22. Graf, H.; Vancea, J.; Hoffmann, H. Single-electron tunneling at room temperature in cobalt nanoparticles. *Appl. Phys. Lett.* **2002**, *80*, 1264–1266. [CrossRef]
23. Li, Z.; Wang, Z.; Xi, S.; Zhao, X.; Sun, T.; Li, J.; Yu, W.; Xu, H.; Herng, T.S.; Hai, X.; et al. Tuning the spin density of cobalt single-atom catalysts for efficient oxygen evolution. *ACS Nano* **2021**, *15*, 7105–7113. [CrossRef]
24. Wu, D.; Tan, Z.; Feng, X.; Anderson, W.A.; Li, Q. Regeneration of cobalt complexes by thermal decomposition and acid treatment for no absorption. *Chem. Eng. J.* **2017**, *315*, 233–242. [CrossRef]
25. Shen, Y.; Deng, J.; Impeng, S.; Li, S.; Yan, T.; Zhang, J.; Shi, L.; Zhang, D. Boosting toluene combustion by engineering co-o strength in cobalt oxide catalysts. *Environ. Sci. Technol.* **2020**, *54*, 10342–10350. [CrossRef] [PubMed]
26. Bessell, S. Support effects in cobalt-based fischer-tropsch catalysis. *Appl. Catal. A Gen.* **1993**, *96*, 253–268. [CrossRef]
27. Bruce, P.G.; Freunberger, S.A.; Hardwick, L.J.; Tarascon, J.M. Li–O_2 and Li–S batteries with high energy storage. *Nat. Mater.* **2012**, *11*, 19–29. [CrossRef]
28. Manthiram, A.; Fu, Y.; Su, Y.S. Challenges and prospects of lithium-sulfur batteries. *Accounts Chem. Res.* **2013**, *46*, 1125–1134. [CrossRef]

29. Yin, H.; He, J.; Xiao, B.; Zhou, M.; Wang, W.; Joao, C.; Chen, Z.; Hou, Z.; Zhang, T.; Yu, Z. Advances and prospects of g-C_3N_4 in lithium-sulfur batteries. *Nano Res. Energy* **2024**, *3*, e9120138. [CrossRef]
30. Feng, S.; Zhong, H.; Song, J.; Zhu, C.; Dong, P.; Shi, Q.; Liu, D.; Li, J.; Chang, Y.C.; Beckman, S.P.; et al. Catalytic activity of co-x (x = s, p, o) and its dependency on nanostructure/chemical composition in lithium-sulfur batteries. *ACS Appl. Energy Mater.* **2018**, *1*, 7014–7021. [CrossRef]
31. Gu, Z.; Cheng, C.; Yan, T.; Liu, G.; Jiang, J.; Mao, J.; Dai, K.; Li, J.; Wu, J.; Zhang, L. Synergistic effect of Co_3Fe_7 alloy and n-doped hollow carbon spheres with high activity and stability for high-performance lithium-sulfur batteries. *Nano Energy* **2021**, *86*, 106111. [CrossRef]
32. Huang, T.; Sun, Y.; Wu, J.; Jin, J.; Wei, C.; Shi, Z.; Wang, M.; Cai, J.; An, X.T.; Wang, P.; et al. A dual-functional fibrous skeleton implanted with single-atomic co-nxdispersions for longevous li-s full batteries. *ACS Nano* **2021**, *15*, 14105–14115. [CrossRef]
33. Sun, X.; Qiu, Y.; Jiang, B.; Chen, Z.; Zhao, C.; Zhou, H.; Yang, L.; Fan, L.; Zhang, Y.; Zhang, N. Isolated fe-co heteronuclear diatomic sites as efficient bifunctional catalysts for high-performance lithium-sulfur batteries. *Nat. Commun.* **2023**, *14*, 291. [CrossRef]
34. Yang, C.; Li, Y.; Peng, W.; Zhang, F.; Fan, X. In situ n-doped CoS_2 anchored on mxene toward an efficient bifunctional catalyst for enhanced lithium-sulfur batteries. *Chem. Eng. J.* **2022**, *427*, 131792. [CrossRef]
35. Li, Y.; Wu, J.; Zhang, B.; Wang, W.; Zhang, G.; Seh, Z.W.; Zhang, N.; Sun, J.; Huang, L.; Jiang, J.; et al. Fast conversion and controlled deposition of lithium (poly)sulfides in lithium-sulfur batteries using high-loading cobalt single atoms. *Energy Storage Mater.* **2020**, *30*, 250–259. [CrossRef]
36. Wang, Y.; Chu, F.; Zeng, J.; Wang, Q.; Naren, T.; Li, Y.; Cheng, Y.; Lei, Y.; Wu, F. Single atom catalysts for fuel cells and rechargeable batteries: Principles, advances, and opportunities. *ACS Nano* **2021**, *15*, 210–239. [CrossRef]
37. Liu, X.; Sui, Y.; Duan, T.; Meng, C.; Han, Y. Monodisperse pt atoms anchored on n-doped graphene as efficient catalysts for co oxidation: A first-principles investigation. *Catal. Sci. Technol.* **2015**, *5*, 1658–1667. [CrossRef]
38. Li, Y.; Zhou, Z.; Yu, G.; Chen, W.; Chen, Z. Co catalytic oxidation on iron-embedded graphene: Computational quest for low-cost nanocatalysts. *J. Phys. Chem. C* **2010**, *114*, 6250–6254. [CrossRef]
39. Therrien, A.J.; Hensley, A.J.R.; Marcinkowski, M.D.; Zhang, R.; Lucci, F.R.; Coughlin, B.; Schilling, A.C.; McEwen, J.S.; Sykes, E.C.H. An atomic-scale view of single-site Pt catalysis for low-temperature CO oxidation. *Nat. Catal.* **2018**, *1*, 192–198. [CrossRef]
40. Tang, Y.; Chen, W.; Zhou, J.; Chai, H.; Li, Y.; Cui, Y.; Feng, Z.; Dai, X. Mechanistic insight into the selective catalytic oxidation for no and co on co-doping graphene sheet: A theoretical study. *Fuel* **2019**, *253*, 1531–1544. [CrossRef]
41. Stokbro, K. First-principles modeling of molecular single-electron transistors. *J. Phys. Chem. C* **2010**, *114*, 20461–20465. [CrossRef]
42. Khademhosseini, V.; Dideban, D.; Ahmadi, M.T.; Ismail, R.; Heidari, H. Impact of hydrogen adsorption on the performance of a single electron transistor utilizing fullerene quantum dots. *ECS J. Solid State Sci. Technol.* **2018**, *7*, M191–M194. [CrossRef]
43. Pronin, I.A.; Plugin, I.A.; Kolosov, D.A.; Karmanov, A.A.; Yakushova, N.D.; Varezhnikov, A.S.; Komolov, A.S.; Lazneva, E.F.; Koroleva, A.V.; Moshnikov, V.A.; et al. Sol-gel derived zno film as a gas sensor: Influence of uv processing versus a thermal annealing. *Sens. Actuators A Phys.* **2024**, *377*, 115707. [CrossRef]
44. Zhao, Q.; Liu, Z.; Xu, Z.; Li, B.; Yang, S. rGO/In_2O_3 heterostructures based gas sensor for efficient ppb-level n-butanol detection. *J. Alloys Compd.* **2024**, *986*, 174154. [CrossRef]
45. Pardeshi, N.M.; Ghuge, R.S.; Birla, P.N.; Chauhan, R.; Bhalekar, S.P.; Shinde, M.D.; Sivalingam, Y.; Kale, R.D.; Rane, S.B. Reduced graphene oxide@bimodal TiO_2 nanocomposites as an efficacious console for room temperature n-butanol gas sensing. *ACS Appl. Electron. Mater.* **2024**, *6*, 4805–4818. [CrossRef]
46. Song, M.K.; Cairns, E.J.; Zhang, Y. Lithium/sulfur batteries with high specific energy: Old challenges and new opportunities. *Nanoscale* **2013**, *5*, 2186–2204. [CrossRef]
47. Nørskov, J.K.; Rossmeisl, J.; Logadottir, A.; Lindqvist, L.; Kitchin, J.R.; Bligaard, T.; Jónsson, H. Origin of the overpotential for oxygen reduction at a fuel-cell cathode. *J. Phys. Chem. B* **2004**, *108*, 17886–17892. [CrossRef] [PubMed]
48. Shen, C.; Xie, J.; Zhang, M.; Andrei, P.; Zheng, J.P.; Hendrickson, M.; Plichta, E.J. A li-li2s4 battery with improved discharge capacity and cycle life at low electrolyte/sulfur ratios. *J. Power Sources* **2019**, *414*, 412–419. [CrossRef]
49. Zhang, H.; Xin, S.; Li, J.; Cui, H.; Liu, Y.; Yang, Y.; Wang, M. Synergistic regulation of polysulfides immobilization and conversion by MOF-derived CoP-HNC nanocages for high-performance lithium-sulfur batteries. *Nano Energy* **2021**, *85*, 106011. [CrossRef]
50. Molavi, R.; Safaiee, R.; Sheikhi, M.H. Oxygen adsorption properties of small cobalt oxide clusters: Application feasibility as oxygen gas sensors. *Phys. Chem. Chem. Phys.* **2020**, *22*, 14889–14899. [CrossRef] [PubMed]
51. Molavi, R.; Safaiee, R.; Sheikhi, M.H.; Hassani, N. Theoretical perspective on co oxidation over small cobalt oxide clusters. *Chem. Phys. Lett.* **2021**, *767*, 138361. [CrossRef]
52. Huang, Z.; Qu, J.; Peng, X.; Liu, W.; Zhang, K.; Wei, X.; Zhong, J. Quantum confinement in graphene quantum dots. *Phys. Status Solidi Rapid Res. Lett.* **2014**, *8*, 436–440. [CrossRef]
53. Zayed, A.O.H.; Daud, M.N.; Zain, S.M. Global structural optimization and growth mechanism of cobalt oxide nanoclusters by genetic algorithm with spin-polarized dft. *J. Alloys Compd.* **2017**, *695*, 2513–2518. [CrossRef]

54. Xie, Y.; Dong, F.; Heinbuch, S.; Rocca, J.J.; Bernstein, E.R. Oxidation reactions on neutral cobalt oxide clusters: Experimental and theoretical studies. *Phys. Chem. Chem. Phys.* **2010**, *12*, 947–959. [CrossRef]
55. Johnson, G.E.; Reveles, J.U.; Reilly, N.M.; Tyo, E.C.; Khanna, S.N.; Castleman, A.W. Influence of stoichiometry and charge state on the structure and reactivity of cobalt oxide clusters with co. *J. Phys. Chem. A* **2008**, *112*, 11330–11340. [CrossRef]
56. Li, M.R.; Chen, J.; Wang, G.C. Reaction mechanism of ethanol on model cobalt catalysts: Dft calculations. *J. Phys. Chem. C* **2016**, *120*, 14198–14208. [CrossRef]

Disclaimer/Publisher's Note: The statements, opinions and data contained in all publications are solely those of the individual author(s) and contributor(s) and not of MDPI and/or the editor(s). MDPI and/or the editor(s) disclaim responsibility for any injury to people or property resulting from any ideas, methods, instructions or products referred to in the content.